PHYSICAL REVIEW B **89**, 104101 (2014)

Lattice dynamics of cubic AuZn from first principles

L. Isaeva, P. Souvatzis, and O. Eriksson
Division of Materials Theory, Department of Physics and Astronomy, Uppsala University, Box 516, SE-751 20 Uppsala, Sweden

J. C. Lashley
Los Alamos National Laboratory, Los Alamos, New Mexico 87545, USA
and Division of Materials Theory, Department of Physics and Astronomy, Uppsala University, Box 516, SE-751 20 Uppsala, Sweden
(Received 9 August 2013; revised manuscript received 17 December 2013; published 4 March 2014)

We study the mechanism of the $B2 \rightarrow R$ martensitic transformation in the shape memory alloy AuZn by means of first-principles theory. Phonon anomalies in the TA$_2$ acoustic branch along the Γ-M $[\xi,\xi,0]$ direction associated with a structural transformation are observed. The calculated Fermi surface of the $B2$ phase of AuZn reveals large portions nested with each other by a translation through a vector $\mathbf{q} = \frac{1}{3}[1,1,0]$ associated with the soft mode. In addition, we find that the $B2$ phase can be stabilized by pressure in the low-temperature limit. The energetic barrier for the $B2 \rightarrow R$ transition is 2 mRy and appears to be near a critical point.

DOI: 10.1103/PhysRevB.89.104101 PACS number(s): 31.15.A−, 63.70.+h, 63.20.Ry

I. INTRODUCTION

A substantial amount of thermodynamic data has been published on the $B2$-phase alloy AuZn. These data include: (1) elastic neutron scattering and inelastic x-ray scattering [1,2], (2) specific heat [3,4] and thermal expansivity [5], (3) electrical transport [3,6], (4) elastic constants and constitutive properties [3], (5) quantum oscillatory phenomena, including de Haas-van Alphen [7,8] and quantum oscillations in the speed of sound [9], (6) Au self-diffusion rates [10–13], (7) angle-resolved and core-level photoemission spectroscopy [14], and (8) a recent Ginzburg-Landau analysis [15]. AuZn is known to undergo a martensitic transformation at $T_c =$ 64 K [2]. Such transformations are known to give rise to bulk scale properties such as recovery of macroscopic shape with temperature, stress, or magnetic field. First discovered nearly a century ago by Ölander [16], this class of materials has become the largest behind the steel industry [17–20].

Martensitic phase transformations are ferroelastic, whereby a spontaneous strain develops below a transformation temperature [21]. Although they commonly occur in many other alloys, only a subset of materials with this phase demonstrates the shape-memory effect. A high-temperature phase transforms to a low-temperature martensitic phase with lower symmetry through softening of a particular phonon branch, usually the TA$_2$ $[\xi,\xi,0]$ for most *bcc* austenitic phases [22]. Early on Zener established the connection between a low shear resistance and lattice distortions in *bcc* and related structures [23]. According to Zener, *bcc*-based structures have the highest elastic shear modulus anisotropy, $A = 2c_{44}/(c_{11} - c_{12})$, where c_{11}, c_{12}, and c_{44} are three independent elastic constants for crystals with cubic symmetry and can be used as an indicator of mechanical instability with respect to (110) $[\bar{1}10]$ shear [24]. It has been shown that the shear instability is linked to alterations in the electronic structure [25,26]. For the AuZn system, the subject of our investigation, the shape-memory effect is connected to a reversible structural transformation from an austenitic $B2$ phase (space group 221, $Pm\bar{3}m$, $O_h{}^1$, Pearson symbol cP2) to a trigonal R (space group 143, $P3$, $C_3{}^1$) martensitic phase containing 27 atoms per primitive cell [1].

The aforementioned data suggest a connection between the band structure and anomalies in the vibrational spectra. In light of these data, we address from first principles the interaction between the electron gas and the lattice vibrations in the vicinity of the structural martensitic transformation in AuZn. It is shown that the transition is nearly critical and phonon softening is accompanied by alterations in the band structure.

II. METHOD

The linear-response (LR) calculations presented in this study are based on density functional theory [27,28] and density functional perturbation theory [29] as implemented in the Quantum ESPRESSO package [30]. These calculations employ ultrasoft (US) pseudopotentials to describe electron-ion interaction [31,32]. Primarily, calculations based on the local density approximation (LDA) [33] have been used, but we also performed calculations based on the generalized gradient approximation (GGA) [34]. A plane-wave basis set with a charge-density cutoff energy up to 800 Ry (10 880 eV) was used to describe the augmented charge of localized d electrons of gold and zinc for both LDA and GGA functionals. Band summation was performed using the "cold smearing" technique by Marzari-Vanderbilt [35] with a broadening of $\sigma = 0.025$ Ry (0.34 eV). A $6 \times 6 \times 6$ q-point mesh resulting in 20 dynamical matrices has been used to perform inverse Fourier transformation and find interatomic force constant matrices in order to calculate phonon frequencies at noncommensurate q points by interpolation.

Direct-force (DF) phonon spectra calculations have been performed using the small displacement method as implemented in PHON package [36]. Force calculations as well as frozen phonon calculations have been performed using density functional theory as implemented within the VASP package [37]. The LDA [38], as well as GGA [34] have been used to describe the exchange-correlation effects. The projector-augmented wave (PAW) potentials have been used with the cutoff energy up to 450 eV. The supercell used in our DF and frozen phonon calculations contains 432 atoms and is obtained by increasing the primitive unit cell 6 times along each of the primitive lattice vectors. Integration over the Brillouin zone was performed using a special k-points technique [39] with $4 \times 4 \times 4$ mesh together with Methfessel-Paxton smearing of $\sigma = 0.200$ eV [40]. Both Fermi surface and bare-static susceptibility calculations are performed by using a single cell with $100 \times 100 \times 100$ and $200 \times 200 \times 200$ Monkhorst-Pack [39] k points, respectively.

III. RESULTS AND DISCUSSION

A. Phonon dispersion relation

To proceed with the analysis of the lattice dynamical properties of $B2$ AuZn, one has to ensure that all the parameters involved into the calculations are converged. Therefore, we have examined the phonon dispersion relations at the experimental lattice parameter 3.13 Å [41] with respect to the cutoff energies, both for the LR US and the DF PAW calculations.

Figure 1 shows the evolution of the phonon dispersion curves of $B2$ AuZn with the cutoff energy. For the US LR calculations the charge-density cutoff was varied [Figs. 1(a) and 1(b)], while for the PAW DF calculations we varied the kinetic cutoff energy [Figs. 1(c) and 1(d)]. The LR US GGA calculations with the cutoff energy of 400 Ry result in a stable TA$_2$ mode along the Γ-M direction, as shown in Fig. 1(a). However, if the cutoff energy is increased up to 800 Ry, the TA$_2$ mode softens and imaginary frequencies appear. The phonon frequency at the M point is $\omega_M^{\mathrm{LR,GGA}} = 0.947$ THz, and at the wave vector $\mathbf{q} = \frac{1}{3}[1,1,0]$ the frequency is $\omega_q^{\mathrm{LR,GGA}} = -0.329i$ THz. If US LDA is used for phonon dispersion calculations [Fig. 1(b)], then at the cutoff energy of 400 Ry the TA$_2$ mode has imaginary frequencies almost along the whole Γ-M direction. When the cutoff energy is increased up to 700 or 800 Ry, the behavior of the TA$_2$ mode mimics the experimental phonon dispersion relation and the imaginary frequency appears close to the wave vector $\mathbf{q} = \frac{1}{3}[1,1,0]$ ($\omega_M^{\mathrm{LR,LDA}} = 0.679$ THz, $\omega_q^{\mathrm{LR,LDA}} = -0.483i$ THz), unlike for the US GGA calculations, where additional imaginary frequency at $\mathbf{q} = \frac{1}{6}[1,1,0]$ persists. The LR calculations are converged when the charge-density cutoff is close to 800 Ry, and both LDA and GGA give imaginary frequencies around $\mathbf{q} = \frac{1}{3}[1,1,0]$ [Figs. 1(a) and 1(b)].

As for the DF calculations, from Figs. 1(c) and 1(d) one can see that for the cutoff energy of 350 eV only PAW LDA picks up the instability along the Γ-M direction $\omega_M^{DF,LDA} = 0.486$ THz, $\omega_q^{DF,LDA} = -0.383i$ THz), while PAW GGA results in positive frequencies along the whole Γ-M direction ($\omega_M^{DF,GGA} = 0.750$ THz, $\omega_q^{DF,GGA} = 0.274$ THz). The result for the PAW GGA potential is in agreement with the phonon dispersion relations obtained in Ref. [15], where the authors have used the DF technique together with the PAW GGA potential and a cutoff energy of 346 eV. One should note here that in Ref. [15] the DF calculations have been performed

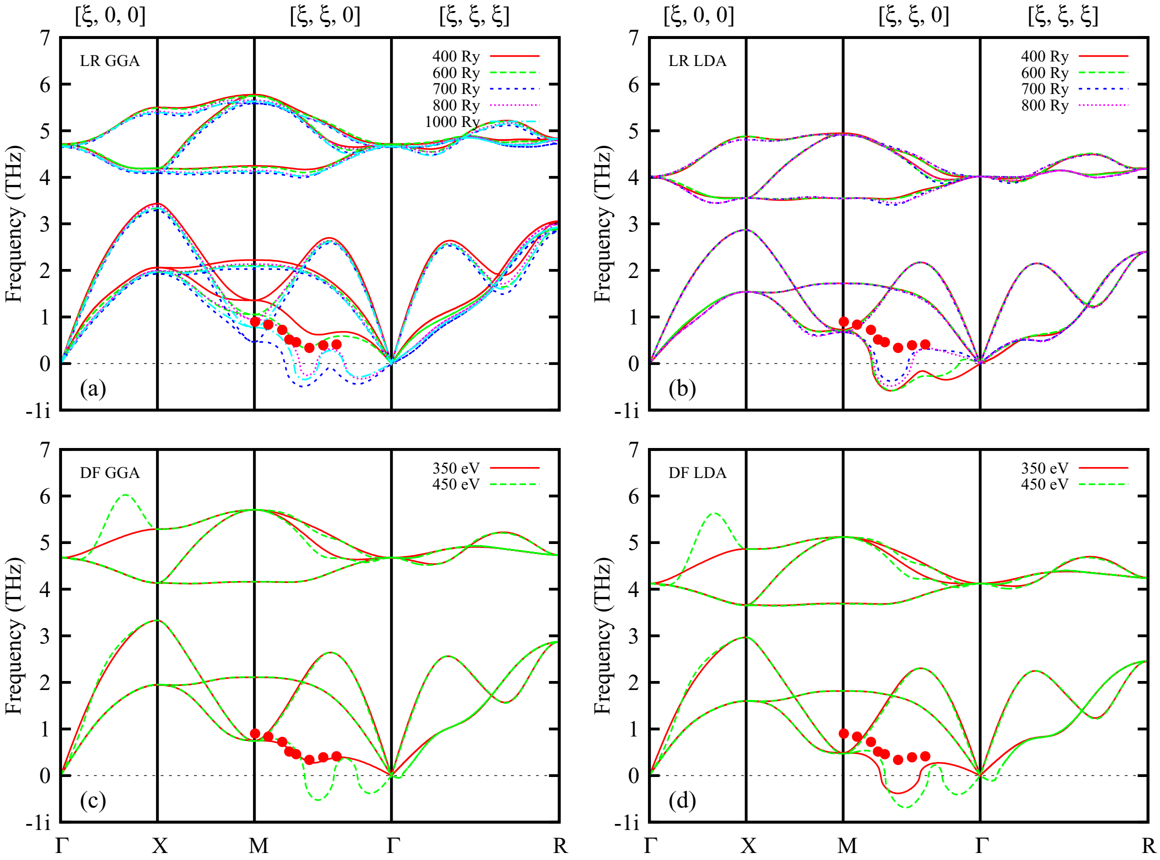

FIG. 1. (Color online) Phonon dispersion relations of $B2$-AuZn calculated using LR (a), (b) and DF (c), (d) methods with different cutoff energies. The DF calculations have been performed using the amplitude of atomic displacement of 0.038 Å. The results of the LR and the DF calculations are shown together with the experimental data (circles) measured using inelastic x-ray scattering at $T = 200$ K [2].

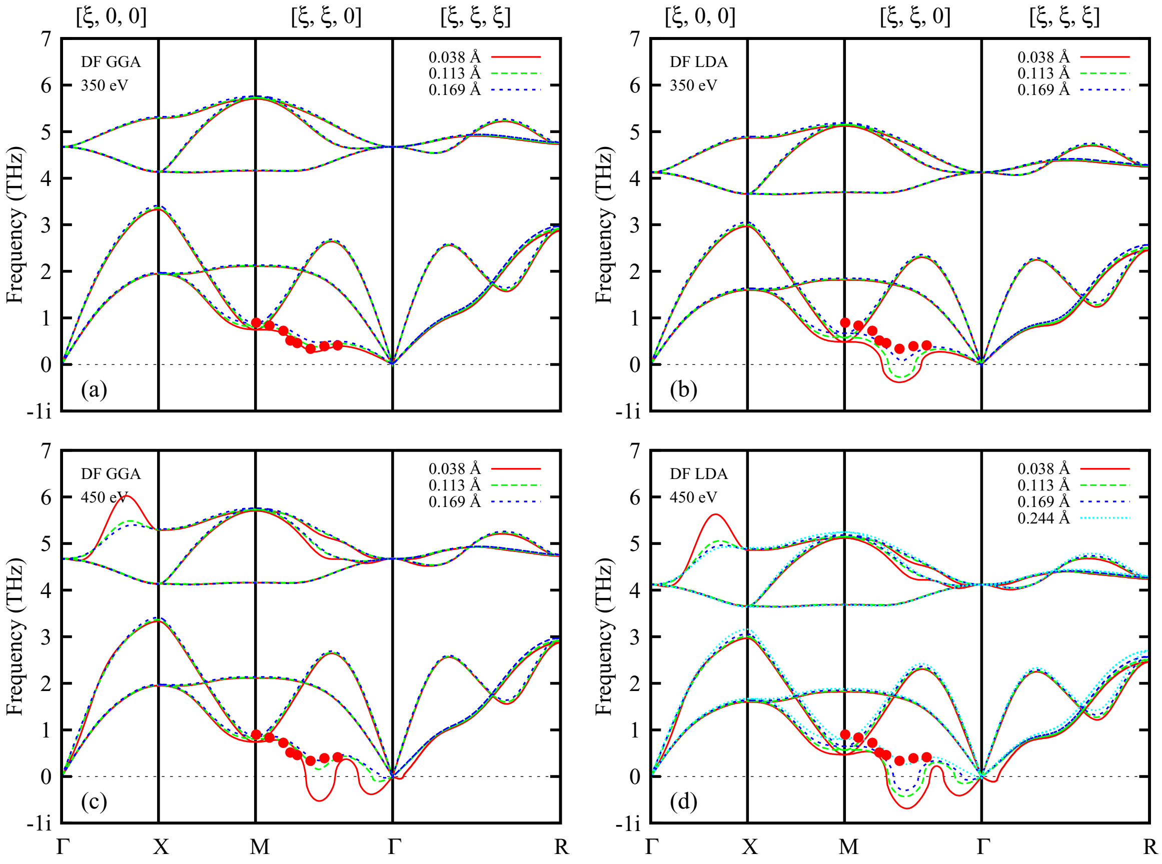

FIG. 2. (Color online) Direct-force phonon dispersion relations of $B2$-AuZn calculated using different values of atomic displacement and cutoff energy. The results are shown together with the experimental data (circles) measured using inelastic x-ray scattering at $T = 200$ K [2].

using a theoretical lattice parameter (3.195 Å) and a 72-atom supercell. We have, therefore, performed additional PAW GGA DF calculations at the lattice parameter 3.195 Å using a $6 \times 6 \times 6$ supercell (432 atoms) and the cutoff energy of 350 eV. The calculation resulted in a soft TA_2 acoustic branch with imaginary frequencies along the Γ-M direction $\omega_q^{DF,GGA} = -0.197i$ THz, unlike Ref. [15], where the authors obtained $\omega_q^{DF,GGA} \approx 0.484$ THz. Coming back to our calculations at the experimental lattice parameter, from Figs. 1(c) and 1(d) one can see that imaginary frequencies appear along the Γ-M direction if the cutoff energy is increased up to 450 eV and that these results are consistent with the data in Figs. 1(a) and 1(b). These calculated phonon dispersion curves show unusual behavior of the optical mode along the Γ-X direction, such as abrupt increase in frequencies up to 5.63 THz (PAW LDA) and 6.02 THz (PAW GGA) and additional imaginary frequencies close to the Γ point along the Γ-M ($\omega^{DF,LDA} = -0.411i$ THz, $\omega^{DF,GGA} = -0.382i$ THz) and Γ-R ($\omega^{DF,LDA} = -0.112i$ THz, $\omega^{DF,GGA} = -0.048i$ THz) directions in TA_2 mode. Assuming that this can be a problem with interpolation, we have performed another PAW GGA calculation, but with a $6 \times 6 \times 6$ k-point grid for the integration over the Brillouin zone. However, the calculation resulted in the same phonon spectrum as in Fig. 1(c) for a 450-eV cutoff energy. On the other hand, the unusual behavior of the optical mode might be associated with very small atomic displacement used for interatomic force constant calculations. We address this issue in detail below.

An important factor that can significantly affect the phonon dispersion relation, while using the DF technique, is the amplitude of atomic displacement used for interatomic force constants calculations. Figure 2 shows the evolution of phonon spectra, calculated using the DF method, with different initial atomic displacements of Au and Zn atoms. We also compare the phonon dispersion curves calculated with the kinetic energy cutoff of 350 and 450 eV. For small atomic displacements at the kinetic cutoff energy of 350 eV [Figs. 1(a) and 1(b)], PAW LDA calculations result in imaginary frequencies along the [ξ,ξ,0] direction, in agreement with the LR results, while PAW GGA gives positive frequencies and no instabilities are present. Further increase in atomic displacement from 0.038 to 0.169 Å in PAW GGA calculation results in insignificant change in phonon frequency at $\mathbf{q} = \frac{1}{3}[1,1,0]$ [Fig. 2(a)]. On the other hand, in the case of LDA PAW, increase of the initial displacements in the calculation of the force constants stiffens the transverse TA_2 acoustic branch, providing a stabilizing effect for the soft mode [Fig. 2(b)]. For an atomic displacement of 0.038 Å, the phonon frequency is $\omega_q^{DF,LDA} = -0.383i$ THz at $\mathbf{q} = \frac{1}{3}[1,1,0]$, for 0.113 Å the frequency is $\omega_q^{DF,LDA} = -0.271i$ THz, and for an atomic displacement of 0.169 Å the phonon frequency is positive $\omega_q^{DF,LDA} = 0.081$ THz. Therefore, the low-energy TA_2 phonon branch along the

[ξ,ξ,0] direction is very sensitive to the amplitude of atomic displacements due to large anharmonic effects. We note, however, that the DF calculations converge towards the LR, when the displacement is gradually reduced. At higher cutoff energy (450 eV) PAW GGA and PAW LDA both result in soft mode with imaginary frequencies along the Γ-M direction if a small displacement is used, which stiffens with the increase of atomic displacement revealing an anharmonic behavior of $B2$ AuZn. Moreover, a change in atomic displacement at the kinetic energy cutoff of 450 eV resolves the numerical problem in the optical part of the spectrum along the Γ-X direction.

Considering all these results, one can see that at a sufficiently large cutoff energy in the DF PAW calculations, both LDA and GGA result in very similar phonon dispersions and are able to pick up the instability along the Γ-M direction, provided sufficiently small displacements are used for the calculation of the dynamical matrix. Both LDA and GGA approximations can be used to describe lattice dynamics of $B2$ AuZn, though GGA must be applied very carefully, so it does not lead to nonconverged results. Overall, we consider the LDA functional to describe best the main feature of the phonon spectrum properly, i.e., soft mode at the wave vector $\mathbf{q} = \frac{1}{3}[1,1,0]$ that is found experimentally. The TA$_2$ acoustic phonon branches along the Γ-M [ξ,ξ,0] direction calculated by means of LR and DF methods are in qualitative agreement with the experimental data measured by inelastic x-ray scattering at $T = 200$ K. Here, by qualitative agreement we mean that theory is able to pick up the instability of the TA$_2$ acoustic branch along Γ-M direction and predict correctly dynamical instability of $B2$ AuZn at low temperatures [2]. The softening along TA$_2$ [ξ,ξ,0] is similar to that observed in NiTi [42], NiAl [43,44], AuCd [45], FePt [46], and other binary Hume-Rothery alloys with electron per atom concentration $e/a = 3:2$.

B. Electron gas properties

Kohn has shown that the lattice vibrations are screened by the conduction electrons in metals leading to a damping of the phonon modes along particular high symmetry directions of the Brillouin zone [47]. Damping can take place whenever there are parallel portions of the Fermi surface resulting in a strong electronic response at the nesting wave vector. Recent de Haas-van Alphen experiments have been performed in stoichiometric AuZn [8]. The Fermi surface of martensitic AuZn has been determined by quantum oscillations in the magnetization [8] and quantum oscillations in the speed of sound [3]. It has been shown that a significant Fermi surface reconstruction takes place during the transformation so that the Fermi surfaces of the parent and the product phases coexist down to 60 mK [8].

To further investigate the microscopical reason for the martensitic transformation in AuZn, we have examined the topology of the Fermi surface of ordered $B2$ AuZn. The fermi surface has been calculated using both US LDA pseudopotential and PAW LDA potential, which resulted in the same topology, though we show only the one calculated with PAW LDA (Fig. 3). The theoretical Fermi surface is derived from two bands that cross the Fermi level and is in favorable agreement with the one previously calculated using the full potential linearized augmented plane wave method (FLAPW) [7]. The Fermi surface does not reveal any particularly complex topology and is consistent of a hole sheet that is centered at the Γ point (sheet in green color), and small, almost flat, electron pockets that are close to the R points (sheets in blue color). These electron pockets are high-frequency pockets and they show up at low magnetic fields and de Haas-van Alphen effect [8]. In Fig. 3 the Fermi surface in the $\mathbf{k_x k_y}$ plane is shown together with the nesting regions where the Fermi surface sheets can be embedded into another by a translation through the vector $\mathbf{q} = \frac{1}{3}[1,1,0]$. This nesting vector coincides with the wave vector at which TA$_2$ mode exhibits a softening. The Fermi surface of AuZn resembles that of Ni-Al, calculated from first principles [25] and measured by Compton scattering [48].

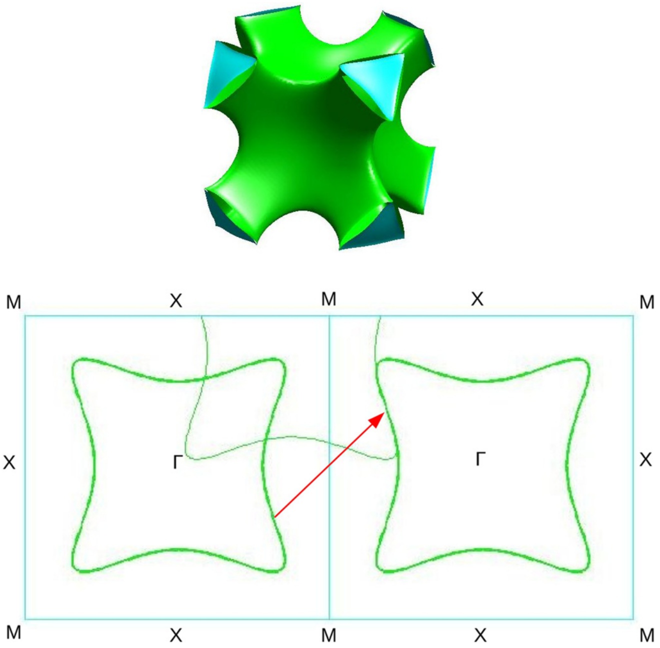

FIG. 3. (Color online) Theoretical Fermi surface of $B2$-AuZn at $T = 0$ K (top). The bottom panel shows a cut through the Fermi surface along (100) plane together with the nesting vector (red arrow) $\mathbf{q} = \frac{1}{3}[1,0,0]$. For the Fermi surface calculations a single cell containing one atom of Au and one atom of Zn has been used together with PAW LDA potentials and $100 \times 100 \times 100$ k-point mesh.

In order to compare our theoretical calculations with de Haas-van Alphen experiments, we have performed an analysis of several extremal orbits of the Fermi surface. The area of extremal orbit obtained from the electronic band in (110) plane (that incorporates the Γ point) is $S_1 = 0.489$ Å^{-2}. For a closed orbit obtained from the electronic band in (100) plane (that incorporates X point) the area is $S_2 = 0.705$ Å^{-2}. Finally, for the closed orbit in (100) obtained from the hole band, the area is $S_3 = 1.431$ Å^{-2}. The measured frequency of de Haas-van Alphen oscillation of 4.7 kT [8] is connected to area of the extremal orbit, S_{exp}, via $S_{\mathrm{exp}} = 2\pi eH/\hbar c$ [49], so we obtain $S_{\mathrm{exp}} = 0.445$ Å^{-2}. Therefore, the area of the first orbit S_1 is in favorable agreement with the experimental S_{exp} with an error $\approx 9.8\%$. The frequency of de Haas-van Alphen oscillations calculated using the theoretical area of extremal orbit, 5.1 kT, is comparable with the measured one, 4.7 kT [8].

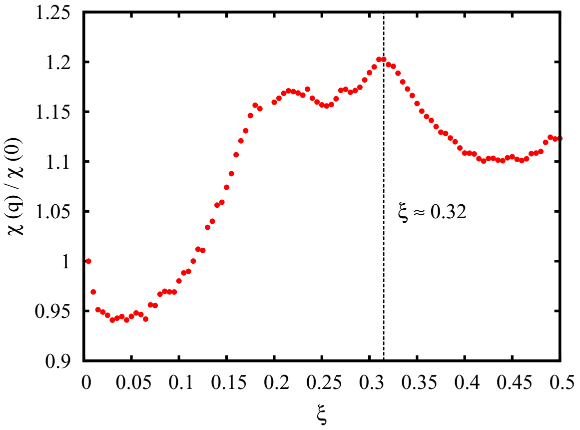

FIG. 4. (Color online) The calculated bare-static susceptibility of $B2$-AuZn as a function of the wave vector $\mathbf{q} = [\xi,\xi,0]$ along the $[\xi,\xi,0]$ direction of the Brilloiun zone, normalized with the value $\chi(0)$ at $\mathbf{q} = 0$. For the susceptibility calculations a single cell has been used together with PAW LDA potentials and dense 200 × 200 × 200 k-point mesh.

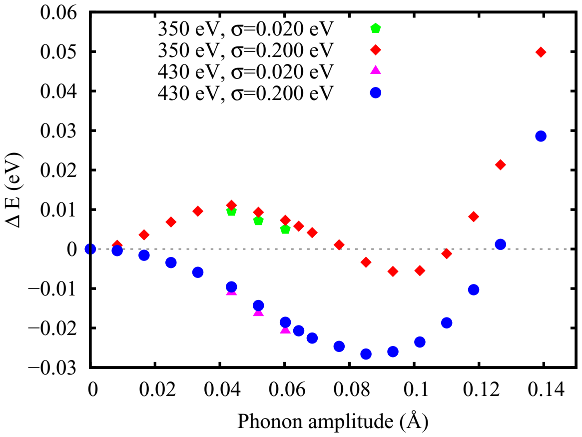

FIG. 5. (Color online) Frozen phonon energy as a function of frozen phonon amplitude. The calculations have been performed using PAW potentials together with a LDA functional and a 4 × 4 × 4 k-point mesh. Energies shown in the figure correspond to the energy per cell containing 432 atoms.

In order to further highlight the effects of nesting, we have also calculated the bare-static susceptibility defined by the Lindhard formula,

$$\chi(\mathbf{q}) = \sum_{\mathbf{k}} \sum_{n,m} \frac{f(\varepsilon_{n,\mathbf{k+q}}) - f(\varepsilon_{m,\mathbf{k}})}{\varepsilon_{n,\mathbf{k+q}} - \varepsilon_{m,\mathbf{k}}}, \qquad (1)$$

where f is the Fermi-Dirac distribution function and $\varepsilon_{m,\mathbf{k}}$ is the energy of the electronic band state with band number m and wave vector $\mathbf{k}$. The temperature at which the martensitic transformation takes place ($T_c = 64$ K) is lower than the Fermi temperature, so instead of the Fermi-Dirac distribution we have used the step function $\Theta(\varepsilon - \varepsilon_F)$ approximation, and Kohn-Sham eigenvalues are summed up over the irreducible part of the Brillouin zone. Figure 4 shows the bare-static susceptibility calculated along the $[\xi,\xi,0]$ direction of the cubic Brillouin zone for $T = 0$ K. We find that the bare-static susceptibility function exhibits a peak along the high-symmetry $[\xi,\xi,0]$ direction of the Brillouin zone. The peak along $[\xi,\xi,0]$ is quite pronounced and occurs at $\mathbf{q} = \frac{1}{3}[1,1,0]$, where phonon softening is observed in the calculation (Fig. 2). Nesting along the $[\xi,\xi,0]$ direction is related to softening of the TA$_2$ branch along the $[\xi,\xi,0]$ direction and is associated with the $B2 \rightarrow R$ phase transition in AuZn. One can expect that a contribution from the electron-phonon coupling matrix elements to the susceptibility will make the peak along $[\xi,\xi,0]$ stronger.

C. Phenomenological approach to $B2 \rightarrow R$ phase transition

Within the context of Ginzburg-Landau theory we have performed LDA PAW frozen phonon energy calculations, where we have used concepts of order parameter, Q, and excess energy, ΔE. The magnitude of the displacement of the TA$_2$ phonon mode can be considered as a primary order parameter driving the $B2 \rightarrow R$ phase transformation in AuZn, similarly to the AuCd system [50]. According to Landau theory of phase transitions one can expand the excess energy of a system, undergoing phase transition, in a Taylor series of the order parameter. Therefore, we calculate the energy of a frozen TA$_2$ phonon (the excess energy in our case) with the eigenvector $\mathbf{q} = \frac{1}{3}[1,1,0]$ excited along $[\xi,\xi,0]$ direction (Fig. 5).

Landau potentials have been calculated with different values of kinetic cutoff energy and bandwidth smearing. As can be seen from Fig. 5, if cutoff energy of 350 eV is used together with a band smearing of 0.200 eV, the Landau potential has a positive curvature at zero phonon amplitudes, which disagrees with the existence of an imaginary TA$_2$ phonon mode along the $[\xi,\xi,0]$ direction [Fig. 1(b)]. The form of the potential is not changed if bandwidth smearing is decreased down to 0.020 eV. However, if the cutoff energy is increased from 350 up to 430 eV, the Landau potential profile changes drastically. The curvature of the potential becomes negative (for both choices of band smearing) and reflects an instability of the $B2$ phase with respect to the R phase at low temperatures, which is consistent with the phonon dispersion curves [Fig. 1(b)].

The form of the excess energy versus order parameter defines the order of the phase transition. If the curvature had been positive for the calculated Landau potential at low values of the ion displacement for the TA$_2$ phonon mode at $\mathbf{q} = \frac{1}{3}[1,1,0]$ and $T = 0$ K, we would have made the conjecture that the transition is most likely first order. In the present case the Landau potential has a negative curvature for low values, and it is difficult to draw any conclusion on the order of the phase transition. However, along with the Landau analysis there is another evidence that can be used to illuminate the order of the phase transition.

Figure 5 shows the measured squared phonon frequencies at the wave vector $\mathbf{q} = \frac{1}{3}[1,1,0]$ versus temperature. The $\omega^2(\mathbf{q})$ versus T dependence is expected to be linear and the extrapolation of the experimental frequencies down to zero gives a transition temperature. Here the extrapolation results in negative $B2 \rightarrow R$ transformation temperature (≈ -150 K). This can be explained if the phase transformation is first order when the phonon amplitude suddenly changes its value from zero to a nonzero value. In this case a soft-mode theory, where the frequency dependence on temperature yields $\omega^2 \approx a(T - T_c)$, does not work. Instead, the dependence is expected

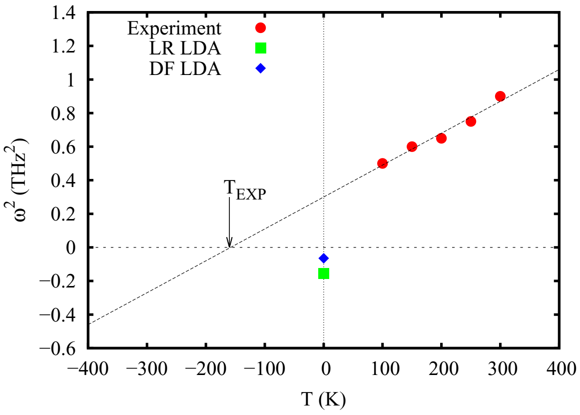

FIG. 6. (Color online) Squared frequencies ω^2 at the wave vector $\mathbf{q} = \frac{1}{3}[1,1,0]$ as a function of temperature T. Measurements (red circles) are performed using inelastic x-ray scattering [51]. The green square corresponds to the US LDA LR calculations, while the blue diamond corresponds to the PAW LDA DF calculations.

to be $\omega^2 \approx a(T + T_c)$. The anharmonic effects push up the soft mode and it has nonzero value at the transition temperature (Fig. 6). The first-order behavior is also manifested by the observation of critical scattering near 64 K [8].

D. Pressure effects

Stabilization of $B2$ AuZn at low temperatures under pressure has also been addressed. We notice first that the experimental lattice parameter 3.13 Å used in our LR phonon spectra calculations results in a hydrostatic pressure of $P_{\rm LDA} = -5.3$ GPa in US LDA, and $P_{\rm GGA} = 8.0$ GPa in US GGA calculations. If perfect agreement between theory and experiment had been achieved as regards the equilibrium volume, the calculated pressures should have been 0 GPa. Hence, the deviation from 0 GPa represents a slight overbinding of the LDA functional and a slight underbinding in the GGA functional. The equilibrium lattice parameters of AuZn in LDA and GGA approximations are 3.09 and 3.19 Å. Phonon frequencies at the M point and at $\mathbf{q} = \frac{1}{3}[1,1,0]$ calculated at these theoretical equilibrium lattice parameters are $\omega_M^{\rm LR,LDA} = 0.800$ THz, $\omega_q^{\rm LR,LDA} = -0.392i$ THz for the US LDA and $\omega_M^{\rm LR,GGA} = 0.948$ THz, $\omega_q^{\rm LR,GGA} = -0.363i$ THz for US GGA calculations. The phonon frequencies calculated at the theoretical equilibrium volumes in both LDA and GGA approaches are imaginary at the $\mathbf{q} = \frac{1}{3}[1,1,0]$ wave vector, as discussed above, which reflects instability of the TA$_2$ mode along the Γ-M directions, and is consistent with the experiment [2].

Next we proceed with the study of evolution of the soft TA$_2$ mode at $\mathbf{q} = \frac{1}{3}[1,1,0]$ wave vector at selected volumes using the LR technique with US GGA and US LDA pseudopotentials. The results of our calculations are summarized in Table I. From this table one can see that the soft TA$_2$ mode stiffens with pressure and stabilizes at a theoretical pressure of 11.2 GPa for US GGA and at 11.5 GPa for for US LDA. A similar effect is observed in α-U where the Σ_4 branch stiffens with pressure [52]. Pressure-stabilized phonon dispersion curves of the $B2$ phase AuZn together with the corresponding phonon densities of states are shown in Fig. 7. Peaks in the theoretical phonon density of states are due to dispersionless phonon modes in acoustical and optical parts of the calculated spectra. Thus, we find that the $B2$ phase should be stable at low temperatures under pressure. The pressure dependence of the transition temperature measured by ac transport confirms our findings [2], where the $B2$ structure is found to be stable at pressures ≈3 GPa. As mentioned above, due to unknown exact form of the exchange-correlation energy, the theoretical equations of states do not represent minima at the experimental lattice parameter 3.13 Å. Therefore, we can not directly compare a theoretical pressure at which $B2$ AuZn is stabilized (11.2 GPa for US GGA and 11.5 GPa for US LDA) with the experimental 3 GPa. However, assuming theoretical pressure versus volume curves are the same as the experimental one, we can recalculate an experimental volume compression at 3 GPa from the theoretical curves. We obtain the experimental volume compression $\Delta V/V = 0.027$ from the US GGA curve, while $\Delta V/V = 0.018$ from the US LDA curve. Next, we notice that in US GGA calculations the $B2$ phase becomes dynamically stable in the pressure range 8.0–11.2 GPa, while in US LDA calculations that range

TABLE I. Evolution of the frequency of TA$_2$ mode ω at $\mathbf{q} = \frac{1}{3}[1,1,0]$ with pressure P. For each pressure we also show corresponding lattice parameter a and volume compression $\Delta V/V$, where V is theoretical equilibrium volume. The calculations are performed within the LR technique.

Functional	a (Å)	P (GPa)	$\Delta V/V$	ω (THz)
GGA	3.163	3.4	0.028	$-0.464i$
	3.130	8.0	0.058	$-0.329i$
	3.110	11.2	0.076	0.269
	3.050	23.0	0.128	0.733
LDA	3.130	-5.3	-0.036	$-0.483i$
	3.060	5.5	0.032	$-0.299i$
	3.030	11.5	0.060	0.180
	2.980	23.8	0.106	0.517

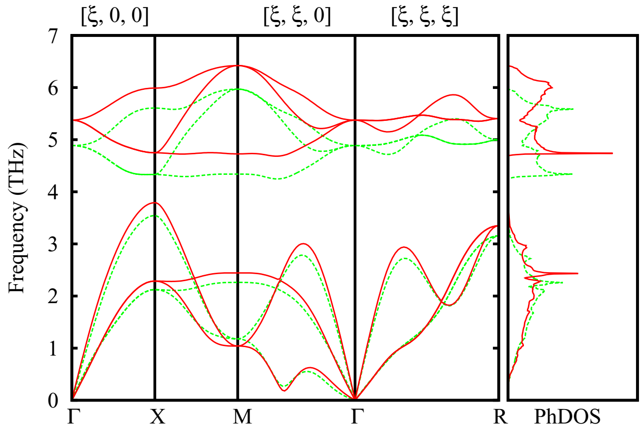

FIG. 7. (Color online) Linear response phonon dispersion relations and phonon density of states calculated at theoretical pressure 11.2 GPa in US GGA (dashed curve) and 11.5 GPa in US LDA (solid curve) calculations.

is 5.5–11.5 GPa. Therefore, we calculate theoretical volume compressions corresponding to these pressure ranges both for GGA and LDA functionals. We obtain $\Delta V/V = 0.019$ for US GGA, and $\Delta V/V = 0.029$ for US LDA. These volume compressions are in favorable agreement with the experimental volume compressions, recalculated from our theoretical data.

One must also notice here that the dip in the TA_2 phonon mode along the Γ-M direction that is found in both US LDA and US GGA calculations is a result of strong electron-phonon coupling that points towards the possibility of superconductivity in the $B2$ phase under pressure, which has recently been observed [53].

IV. SUMMARY

We present a comprehensive theoretical study of the microscopic mechanism behind the martensitic transformation in AuZn, where both the vibrational spectrum and the Fermi surface are addressed. Different *ab initio* approaches have been used to describe the lattice dynamics of AuZn at low temperatures. It has been emphasized that high cutoff energies, such as 800 Ry in US GGA and 450 eV in PAW GGA calculations, have to be used in order to capture the instability of TA_2 mode along the Γ-M direction. In the case of LDA one can use smaller cutoff energies, e.g., 700 Ry for US pseudopotentials and 450 eV for PAW potentials. At a sufficiently large cutoff energy both GGA and LDA functionals, in US LR and PAW DF calculations, result in a very similar phonon dispersions and are able to pick up the instability along the Γ-M direction. We have also shown that careful description of frozen TA_2 phonon mode, responsible for the $B2 \rightarrow R$ transition, at $\mathbf{q} = \frac{1}{3}[1,1,0]$ requires higher cutoff energies compared to the phonon dispersion calculations if the PAW LDA potential is used. In the case of AuZn an insufficient cutoff energy can result in Landau potential profile inconsistent with the phonon spectrum. From the experimental $\omega^2(\mathbf{q})$ versus T dependence we conclude that the $B2 \rightarrow R$ transition is of first order.

Our studies show that AuZn is anharmonic, in the sense that phonon modes which are imaginary for smaller displacements of atoms become real for larger displacements. The topology of the Fermi surface has been investigated and it has been shown that Fermi surface nesting along $\mathbf{q} = \frac{1}{3}[1,1,0]$ is coupled to the phonon softening along the Γ-M direction of the cubic Brillouin zone. The contribution of the bare-static susceptibility to electron-phonon interaction has also been investigated. We have shown that phonon softening occurs at the same wave vector $\mathbf{q} = \frac{1}{3}[1,1,0]$ where the susceptibility exhibits a maximum. The peak in the bare-static susceptibility combined with the soft TA_2 phonon mode are likely to be the driving mechanism for the martensitic transition in AuZn. We also suggest that the strong electron-phonon coupling is likely to be the operative mechanism for martensitic $B2 \rightarrow R$ transformation in AuZn. From the measured temperature dependence of phonon frequencies at the $\mathbf{q} = \frac{1}{3}[1,1,0]$ wave vector we suggest that the transformation is of first order. $B2$ AuZn is stabilized at low temperatures at a theoretical pressure of 11.2 GPa in US GGA and 11.5 GPa in US LDA LR calculations, and we suggest that the $B2$ phase of AuZn under pressure can be the global ground state at low temperatures. Large softening along $[\xi,\xi,0]$ direction can arise due to strong electron-phonon coupling and could give rise to superconductivity similar to charge-density wave materials.

ACKNOWLEDGMENTS

L.E., P.S., and O.E. acknowledge VR, ERC (Grant No. 247062), eSSENCE, and KAW for financial support. Calculations done under a contract from SNAC. Experimental work was performed at the Los Alamos National Laboratory under the auspices of the United States Department of Energy.

---

[1] T. Makita, *et al.*, Phys. B **213**, 430 (1995).
[2] J. C. Lashley *et al.*, Phys. Rev. Lett. **101**, 135703 (2008).
[3] T. W. Darling *et al.*, Philos. Mag. B **82**, 825 (2002).
[4] J. C. Lashley *et al.* J. Chem. Thermodyn. **34**, 251 (2002).
[5] J. C. Lashley *et al.*, Mater. Trans. **47**, 587 (2006).
[6] H. Pops and T. B. Massalski, Trans. Metall. Soc. AIME **233**, 728 (1965).
[7] R. D. McDonald *et al.*, J. Phys. Condens. Matter **17**, L69 (2005).
[8] P. A. Goddard, J. Singleton, R. D. McDonald, N. Harrison, J. C. Lashley, H. Harima, and M.-T. Suzuki, Phys. Rev. Lett. **94**, 116401 (2005).
[9] J. C. Lashley *et al.*, Phys. Rev. B **75**, 205119 (2007).
[10] D. Gupta and D. S. Lieberman, Phys. Rev. B **4**, 1070 (1971).
[11] R. N. Jeffery, Phys. Rev. B **6**, 4432 (1972).
[12] M. Van Dal, Philos. Mag. A **82**, 943 (2002).
[13] C. R. Kao and Y. A. Chang, Intermetallics **1**, 237 (1993).
[14] J. C. Lashley *et al.* (unpublished).
[15] M. Sanati, R. C. Albers, T. Lookman, and A. Saxena, Phys. Rev. B **88**, 024110 (2013).
[16] A. Ölander, J. Am. Chem. Soc. **54**, 3819 (1932).
[17] K. Otsuka and T. Kakeshita, MRS Bulletin **27**, 91 (2002).
[18] T. Kakeshita and K.Ulakko, MRS Bulletin **27**, 105 (2002).
[19] T. W. Duerig, MRS Bulletin **27**, 101 (2002).
[20] G. B. Olson, Mat. Sci. Eng. A, **273**, 11 (1999).
[21] E. K. H. Salje, Ferroelectrics **104**, 111 (1990).
[22] G. Grimvall *et al.*, Rev. Mod. Phys. **84**, 945 (2012).
[23] C. Zener, Phys. Rev. **71**, 846 (1947).
[24] A. Planes and L. Mañosa, Sol. St. Phys. **55**, 159 (2001).
[25] G. L. Zhao and B. N. Harmon, Phys. Rev. B **45**, 2818 (1992).
[26] G. L. Zhao and B. N. Harmon, Phys. Rev. B **48**, 2031 (1993).
[27] P. Hohenberg and W. Kohn, Phys. Rev. **136**, B864 (1964).
[28] W. Kohn and L. J. Sham, Phys. Rev. **140**, A1133 (1965).
[29] S. Baroni *et al.*, Rev. Mod. Phys. **73**, 515 (2001).
[30] P. Giannozzi *et al.*, J. Phys. Condens. Matter **21**, 395502 (2009).
[31] A. M. Rappe, K. M. Rabe, E. Kaxiras, and J. D. Joannopoulos, Phys. Rev. B **41**, 1227(R) (1990).
[32] D. Vanderbilt, Phys. Rev. B **41**, 7892 (1990).
[33] J. P. Perdew and A. Zunger, Phys. Rev. B **23**, 5048 (1981).
[34] J. P. Perdew, K. Burke, and M. Ernzerhof, Phys. Rev. Lett. **77**, 3865 (1996).

[35] N. Marzari, D. Vanderbilt, A. DeVita, and M. C. Payne, Phys. Rev. Lett. **82**, 3296 (1999).
[36] D. Alfe, Comput. Phys. Commun. **180**, 2622 (2009).
[37] G. Kresse and J. Furthmuller, Phys. Rev. B **54**, 11169 (1996).
[38] D. M. Ceperley and B. J. Alder, Phys. Rev. Lett. **45**, 566 (1980).
[39] H. Monkhorst and J. Pack, Phys. Rev. B **13**, 5188 (1976).
[40] M. Methfessel and A. T. Paxton, Phys. Rev. B **40**, 3616 (1989).
[41] K. Krompholz and A. Weiss, Ber. Bunsenges. Phys. Chem. **82**, 334 (1978).
[42] H. Tietze, M. Mullner, and B. Renker, J. Phys. C **17**, L529 (1984).
[43] S. M. Shapiro, B. X. Yang, Y. Noda, L. E. Tanner, and D. Schryvers, Phys. Rev. B **44**, 9301 (1991).
[44] E. I. Isaev *et al*., Solid State Commun. **129**, 809 (2004).
[45] T. Ohba, Phase Transitions **69**, 289 (1999).
[46] J. Kästner *et al*., Eur. Phys. J. B **10**, 641 (1999).
[47] W. Kohn, Phys. Rev. Lett. **2**, 393 (1959).
[48] S. B. Dugdale, R. J. Watts, J. Laverock, Z. Major, M. A. Alam, M. Samsel-Czekała, G. Kontrym-Sznajd, Y. Sakurai, M. Itou, and D. Fort, Phys. Rev. Lett. **96**, 046406 (2006).
[49] N. W. Ashcroft and N. D. Mermin, *Solid State Physics* (Saunders College Publishing, Philadelphia, 1976).
[50] G. R. Barsch, Mater. Sci. Forum **327-328**, 367 (2000).
[51] J. C. Lashley and S. M. Shapiro (unpublished).
[52] S. Raymond *et al*., Phys. Rev. Lett. **107**, 136401 (2011).
[53] J. C. Lashley *et al*. (unpublished).